# Orbital Ingredients and Persistent Dirac Surface State for the Topological Band Structure in $FeTe_{0.55}Se_{0.45}$

Y.-F. Li,[1,2,3,*] S.-D. Chen,[1,2,3,4,*] M. García-Díez,[5,6] M. I. Iraola,[5,7] H. Pfau,[1,8,9] Y.-L. Zhu,[9] Z.-Q. Mao,[9] T. Chen,[10] M. Yi,[10] P.-C. Dai,[10] J. A. Sobota,[1] M. Hashimoto,[11] M. G. Vergniory,[5,12,†] D.-H. Lu,[11,‡] and Z.-X. Shen[1,2,3,§]

[1]*Stanford Institute for Materials and Energy Sciences, SLAC National Accelerator Laboratory, Menlo Park, California 94025, USA*
[2]*Department of Applied Physics and Physics, Stanford University, Stanford, California 94305, USA*
[3]*Geballe Laboratory for Advanced Materials, Stanford University, Stanford, California 94305, USA*
[4]*Department of Physics, University of California, Berkeley, California 94720, USA*
[5]*Donostia International Physics Center, 20018 Donostia-San Sebastián, Spain*
[6]*Physics Department, University of the Basque Country (UPV/EHU), Bilbao, Spain*
[7]*Institute for Theoretical Solid State Physics, IFW Dresden, Helmholtzstrasse 20, Dresden, Germany*
[8]*Advanced Light Source, Lawrence Berkeley National Laboratory, Berkeley, California 94720, USA*
[9]*Department of Physics, Pennsylvania State University, University Park, Pennsylvania 16802, USA*
[10]*Department of Physics and Astronomy, Rice University, Houston, Texas 77005, USA*
[11]*Stanford Synchrotron Radiation Lightsource, SLAC National Accelerator Laboratory, Menlo Park, California 94025, USA*
[12]*Max Planck Institute for Chemical Physics of Solids, Dresden D-01187, Germany*

(Received 22 August 2023; revised 2 April 2024; accepted 25 April 2024; published 11 June 2024)

$FeTe_{0.55}Se_{0.45}$ (FTS) occupies a special spot in modern condensed matter physics at the intersections of electron correlation, topology, and unconventional superconductivity. The bulk electronic structure of FTS is predicted to be topologically nontrivial due to the band inversion between the $d_{xz}$ and $p_z$ bands along $\Gamma$-$Z$. However, there remain debates in both the authenticity of the Dirac surface states (DSSs) and the experimental deviations of band structure from the theoretical band inversion picture. Here we resolve these debates through a comprehensive angle-resolved photoemission spectroscopy investigation. We first observe a persistent DSS independent of $k_z$. Then, by comparing FTS with FeSe, which has no band inversion along $\Gamma$-$Z$, we identify the spectral weight fingerprint of both the presence of the $p_z$ band and the inversion between the $d_{xz}$ and $p_z$ bands. Furthermore, we propose a renormalization scheme for the band structure under the framework of a tight-binding model preserving crystal symmetry. Our results highlight the significant influence of correlation on modifying the band structure and make a strong case for the existence of topological band structure in this unconventional superconductor.

DOI: 10.1103/PhysRevX.14.021043

Subject Areas: Condensed Matter Physics, Strongly Correlated Materials, Superconductivity

The iron-based superconductors (IBSs) have substantially contributed to our understanding of electron correlation and unconventional superconductivity [1–10]. More recently, this material system has also emerged as one of the leading platforms for the possible realization of topological superconductivity [11–19]. Among all proposed topological superconductors in IBSs, $FeTe_{0.55}Se_{0.45}$ (FTS) is the most investigated system. From density functional theory (DFT) calculations, the topological nature of FTS is predicted to arise from the inversion between the bulk $p_z$ and $d_{xz}$ bands along $\Gamma$-$Z$ [20]. However, unlike weakly correlated topological materials such as $Bi_2Te_3$, where theoretical predictions are usually reliable [21,22], experimental inputs are indispensable for a comprehensive understanding of FTS because of its strong electron correlation. Scanning tunneling spectroscopy experiments pioneered in identifying the possible topological superconductivity by observing zero-energy peaks at the vortex centers, which can be interpreted as Majorana zero-energy modes [23–28]. However, the

*These authors contributed equally to this work.
†maia.vergniory@cpfs.mpg.de
‡dhlu@slac.stanford.edu
§zxshen@stanford.edu

absence of zero-energy peaks in some of the vortex cores requires further investigation [26]. In angle-resolved photoemission spectroscopy (ARPES) experiments, Zhang *et al.* first observed a Dirac-cone-like feature at a single photon energy and interpreted it as the Dirac surface state (DSS) [29]. Nevertheless, a later experiment reported that this feature exists only at certain photon energies, and speculated that it might originate from a bulk band instead of the DSS [30]. More importantly, the measured $k_z$ dispersions [31–33] differ significantly from DFT predictions [12,20,29], with no direct evidence for either the $p_z$ orbital or the band inversion in the bulk-band structure. These observations challenge the claimed topological superconductivity in FTS. To resolve these conflicts, we perform systematic ARPES measurements.

We start by assigning the observed features near the Brillouin zone (BZ) center in FTS to the corresponding electronic states. According to band structure calculations [20], the states close to Fermi level are Fe $d_{xz}$, $d_{yz}$, $d_{xy}$, and Se/Te $p_z$. The intensities of the three Fe $t_{2g}$ orbitals are strongly affected by matrix element effects near the BZ center [5,34–38]. Along the Γ-$M$ direction under $p$ ($s$) polarization, only the $d_{yz}$ ($d_{xz}$) orbital is enhanced while the other $t_{2g}$ orbitals are suppressed [see Supplemental Material

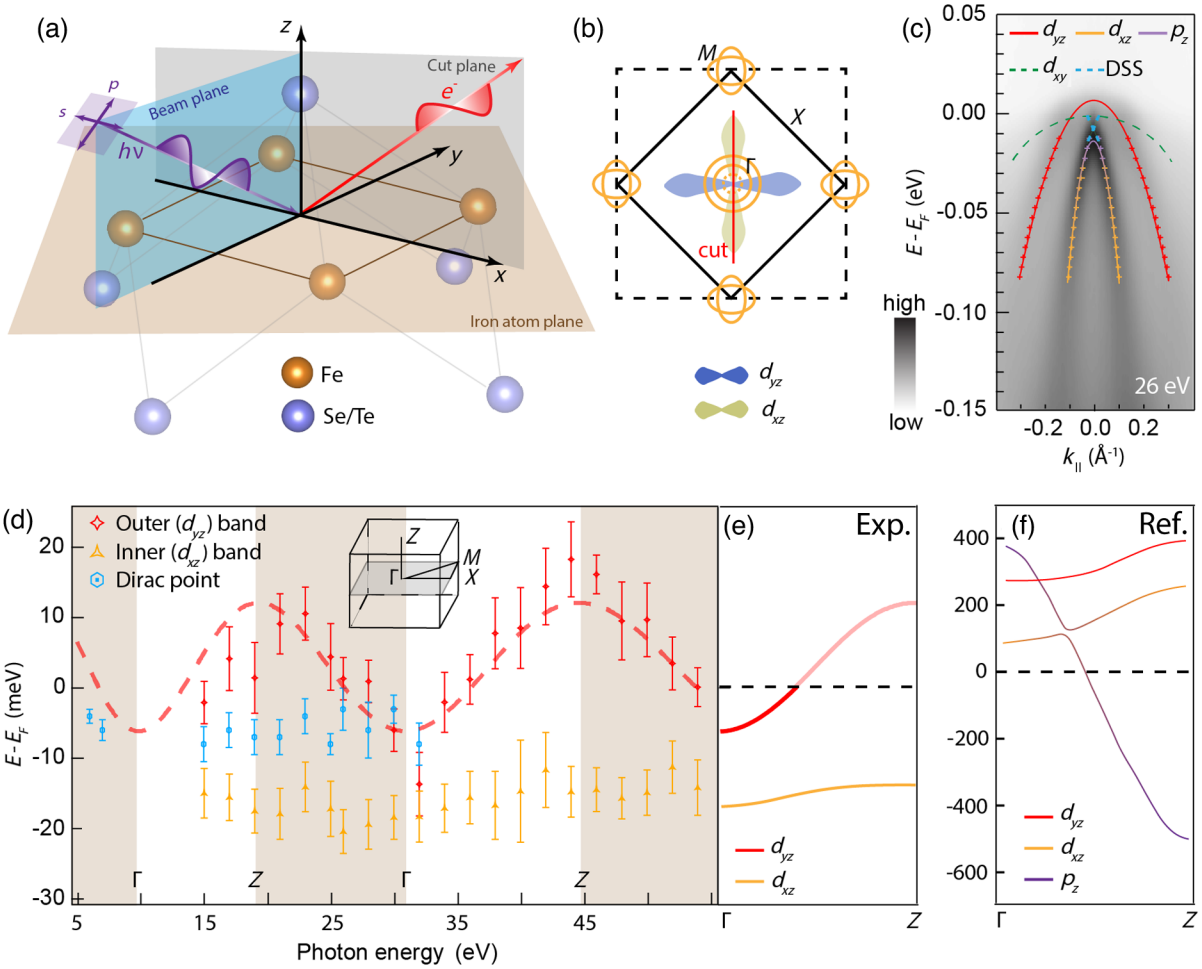


FIG. 1. ARPES experimental geometry and band dispersions along Γ-$Z$. (a) Schematic of the ARPES experimental geometry. The electric field of $s$ and $p$ polarization are normal and parallel to the beam plane, respectively. (b) Schematic of the cut geometry along Γ-$M$. Black solid and dashed lines show 2-Fe and 1-Fe Brillouin zones (BZ), respectively. Orange solid lines mark two holelike pockets near the zone center ($d_{yz}$ and $d_{xy}$ bands) and two electron pockets at $M$. The orange dashed line marks one holelike band closely below $E_F$ ($d_{xz}$ band). Green and blue patterns show the shapes of $d_{xz}$ and $d_{yz}$ orbitals projected on the $xy$ plane, respectively. (c) A representative ARPES spectra along Γ-$M$ at $h\nu = 26$ eV with $p$ polarization. Crosses show the band dispersion extracted from momentum distribution curve (MDC) analysis. Red and purple-orange solid lines are parabolic fits to the $d_{yz}$ and $p_z$-$d_{xz}$ bands, respectively. Green and blue dashed lines are guides to the eye for the $d_{xy}$ band and Dirac surface state (DSS), respectively. (d) Photon energy dependence of low energy electronic states. The red dashed guide to the eye indicates the periodicity of the outer band top along Γ-$Z$. Inset shows the 3D BZ and high symmetry points. (e),(f) Schematic of the bulk band dispersion along Γ-Z. The dispersion extracted from (d) and adapted from Ref. [20] are shown in (e) and (f), respectively.

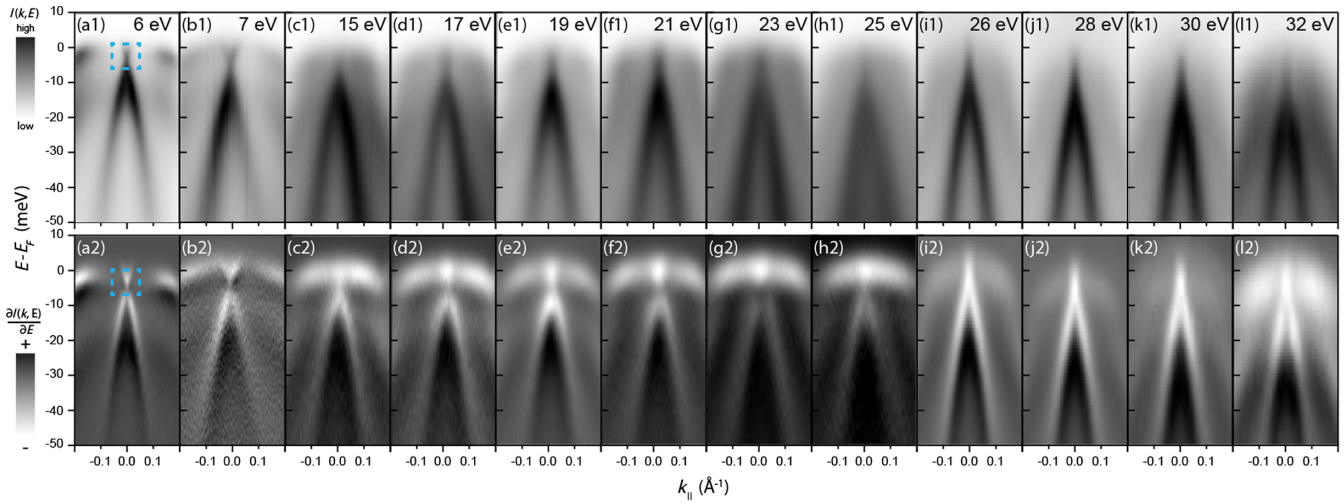


FIG. 2. Dirac surface state at different photon energies. (a1)–(l1) ARPES spectra over a wide range of photon energies. (a2)–(l2) The first-energy-derivative spectra in (a1)–(l1). Blue dashed boxes indicate the energy-momentum window containing the DSS signal. 6–7 eV spectra are taken with lasers. 15–25 and 26–32 eV spectra are taken with synchrotron light source at two complementary beam lines. All cuts go through BZ center. Detailed analysis on DSS is presented in Supplemental Material Fig. S2 and S3 [39].

(SM) Secs. 1 and 6 for details [39] ]. Figure 1(c) shows a representative ARPES spectrum along Γ-$M$ in-plane direction under $p$ polarization at photon energy $h\nu = 26$ eV [the corresponding data under $s$ polarization are shown in Fig. S1(b) in SM [39] ]. Similar to the other IBSs in the 11 family [5,35–37], we observe three hole bands near $E_F$. The outer band [Fig. 1(c), red line] is of $d_{yz}$ character and is observed only under $p$ polarization. The $d_{xy}$ orbital produces a flat holelike band [Fig. 1(c), green line] with weak intensity, which can be more clearly identified in the second-energy-derivative spectra [Fig. S1(c), green dashed line]. The inner band is typically identified with the $d_{xz}$ orbital in 11-family compounds and has weak (strong) intensity under $p$ ($s$) polarizations. Surprisingly, the inner band here [Fig. 1(c), orange-purple line] has strong intensity under both $p$ and $s$ polarizations, which we will explain later.

We perform parabolic fits to the in-plane dispersions of bulk bands obtained from momentum distribution curve (MDC) analysis (see SM Sec. II for details [39]). The extracted band top positions are plotted in Fig. 1(d) as a function of photon energy (or $k_z$, with fitted inner potential $V_0 \approx 11.3$ eV; see SM Sec. III for details). The outer band top shows periodic oscillations spanning a ∼20 meV range [red guideline in Fig. 1(d)], while the inner band shows almost no $k_z$ dispersion within measurement uncertainties, consistent with previous reports [31–33]. Figures 1(e) and 1(f) show the schematic band $k_z$ dispersion extracted from experiments and the DFT calculations in Ref. [20], respectively. Contrary to the DFT calculations, first glance revealed neither a $k_z$-dispersive $p_z$ band nor band inversion, with an additional inconsistency in fermiology. Indeed, the $k_z$ dispersion of the inner band is almost identical to those in other 11-family compounds without band inversion [40], raising questions on the predicted topological nature in FTS.

To resolve the discrepancies, in the following, we will report three observations unique to FTS to support a topological band structure: (i) the $k_z$-independent DSS, (ii) the presence of $p_z$ orbital character in the inner band, and (iii) the orbital character crossover hinted by the spectral weight variations.

We first demonstrate the $k_z$-independent DSS. Figures 2(a1)–2(l1) show the enlarged spectra near $E_F$ over a wide range of photon energies, taken with 6 nd 7 eV lasers and synchrotron photons between 15 and 32 eV. Our result is consistent with the first report of the DSS at $h\nu = 7$ eV [29], but contains data covering the entire Γ-$Z$ trajectory. Contrary to the previous photon-energy-dependence study [30], we find that the DSS feature persists throughout the photon energy range in Figs. 2(a1)–2(l1) in the energy-momentum window indicated by the blue dashed box [Figs. 2(a1) and 2(a2)]. The first-energy-derivative plots in Figs. 2(a2)–2(l2) better highlight the DSS at some photon energies. We note that the DSS feature exists in a very narrow momentum and energy window, and consequently requires careful measurements with optimized measurement alignment, small beam spot size, and high instrument resolution. Following an earlier study [33], we further perform a quantitative analysis to confirm the $k_z$-independent DSS signal. We fit MDCs between −14 meV and $E_F$, and extract the widths of the MDC peaks associated with the DSS as a function of energy (see SM Sec. IV for details [39]). The MDC widths are expected to reach minimum at the binding energy of the Dirac point. In Fig. 1(d), we show that the binding energy of the Dirac point stays fixed as a function of photon energy, despite the ∼20 meV $k_z$ dispersion of the $d_{yz}$ band. The 2D nature of the Dirac-cone-type feature confirms its surface state origin and rules out the interpretation of the $p_z$

band bottom in an earlier study [41]. Above 32 eV, the DSS signal becomes hard to identify because of the deteriorated in-plane momentum resolution and a potential matrix element suppression of the $p_z$ atomic orbital component (to be discussed below) [42]. Nevertheless, the photon energy range presented here is large enough to cover the entire Γ-$Z$ range [Fig. 1(d)]. Therefore, our data support the DSS interpretation and exclude the possibility that the Dirac-cone-like dispersion comes from the subtle bulk-band crossing at specific $k_z$ [30].

Having confirmed the existence of DSS, we now look for its bulk correspondence by first searching for the evidence of the $p_z$ orbital that participates in the band inversion with the $d_{xz}$. In Fig. 3, we compare the spectra of FTS with those of FeSe, a closely related compound predicted to have no band inversion along Γ-$Z$ [20]. Figures 3(a)–3(e) and 3(g)–3(i) show spectra of FTS and FeSe along the Γ-$M$ direction at different photon energies, respectively. We first compare the band intensity as a function of in-plane momentum ($k_\parallel$). Along the Γ-$M$ direction under $p$ polarization, the matrix element of the $d_{xz}$ is suppressed near $k_\parallel = 0$, while the matrix elements of $d_{yz}$ and $p_z$ orbitals remain large (Figs. S10 and S12 [39]). Experimentally, we indeed find that the inner band of FeSe, whose orbital character is dominantly $d_{xz}$ without considering the spin-orbit coupling (SOC) [40], has suppressed intensity near the inner band top ($k_\parallel = 0$) [Figs. 3(g)–3(i)]. In contrast, the inner band of FTS shows maximal intensity at $k_\parallel = 0$ [Figs. 3(a)–3(e)]. This indicates the presence of either the $d_{yz}$ or the $p_z$ orbital component near the inner band top.

To better understand this orbital component, we further look into the spectral weight contrast between the inner and outer bands. We quantify the contrast by defining the spectral weight ratio (SWR) as the ratio between the average intensities in region 2 [orange bar in Fig. 3(a) sampling the inner band] and region 1 [red bars in Fig. 3(a)

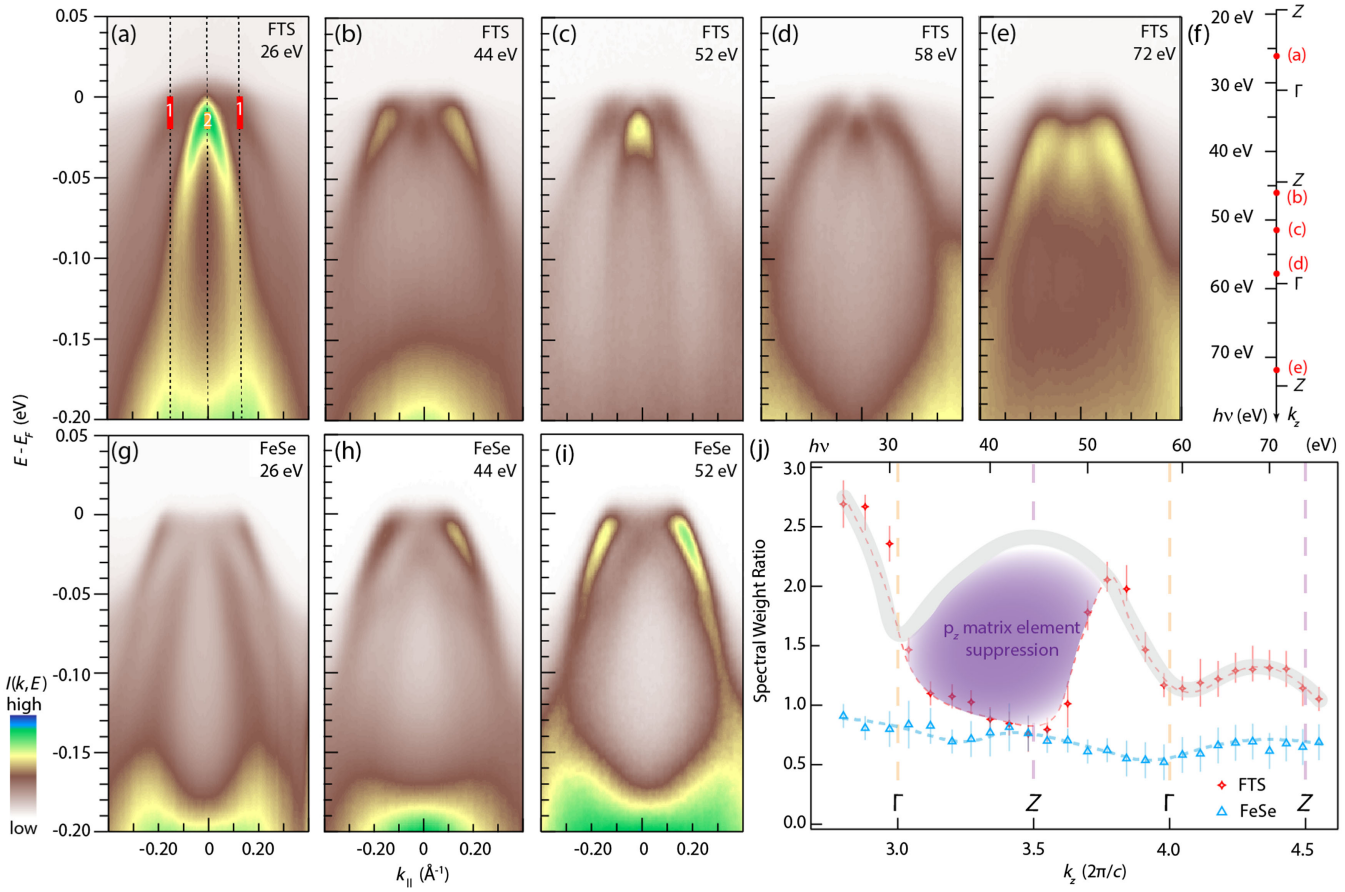


FIG. 3. Spectral weight modulation in FTS. (a)–(e) FTS spectra cut along Γ-$M$ taken at $h\nu$ = (a) 26 eV, (b) 44 eV, (c) 52 eV, (d) 58 eV, and (e) 70 eV, respectively. The red and orange bars in (a) indicate region 1 and region 2 in spectral weight analysis, respectively. (f) Correspondence between photon energy and $k_z$ for FTS. Red dots mark photon energies in (a)–(e). (g)–(i) FeSe spectra cut along Γ-$M$ taken at (g) 26 eV, (h) 44 eV, and (i) 52 eV, respectively. (j) The spectral weight ratio (SWR) as a function of photon energy for FTS and FeSe. The $k_z$ values apply to FTS only. Orange and purple dashed lines indicate Γ and $Z$ points in FTS, respectively. The gray line is a guide to the eye for the expected oscillatory behavior. The purple shaded area marks the anomalous matrix element depression. All cuts are along Γ-$M$ taken under $p$ polarization.

sampling the outer band; see SM Sec. V for details [39] ]. The SWRs for the Γ-$M$ cut are plotted in Fig. 3(j) as a function of photon energy (see Figs. S6 and S8 for the raw spectra [39]). For FeSe, the SWR remains almost constant with tiny modulations. This behavior is expected because the dominant orbital components for the inner and outer bands in FeSe are $d_{xz}$ and $d_{yz}$, respectively [40], and the matrix element ratio between these two orbital components is roughly photon-energy independent (Fig. S10 [39]). In contrast, the SWR for FTS shows strong and intricate modulations, echoing the in-plane intensity distribution anomaly and consistent with the $k_z$-dependent mixing of either the $d_{yz}$ or the $p_z$ orbital components in the inner $d_{xz}$ band. In the case of $d_{yz}$ mixing with $d_{xz}$, the SWR modulation is only expected in the data collected along the Γ-$M$ but not the Γ-$X$ direction, because these two orbitals have the similar matrix elements along Γ-$X$ as required by symmetry [Fig. S5(d); also see SM Sec. 5 for details [39] ]. However, we also observe a similar SWR modulation in data taken along Γ-$X$ (see SM Sec. V for details). Therefore, the SWR modulations can only arise from the hybridization between the $d_{xz}$ and $p_z$ orbitals near the inner band top. The contrasting behaviors in FeSe and FTS highlight the importance of the Te $5p_z$ orbital: It introduces strong interlayer hopping and brings the $p_z$ dispersion across the Fe $t_{2g}$ bands [20], eventually leading to a significant mixing of the $p_z$ orbital character into the inner Fe $d_{xz}$ band.

Having established the $p_z$ orbital component, we now further look for evidence of $d_{xz}$-$p_z$ orbital character crossover near the inner band top as a function of $k_z$—a natural consequence of the bulk-band inversion. The SWR in FTS in Fig. 3(j) can be understood as a product of two effects: an oscillatory behavior by the orbital character change (gray guide to the eye) and an anomalous depression of the photoemission matrix element near 40 eV (purple shaded area). The overall oscillatory behavior suggests that the spectral weight of the inner band reaches the maximum at $Z$ and the minimum at Γ. This implies a $d_{xz}$-$p_z$ crossover of the orbital character going from Γ to $Z$ at the inner band top since the $p_z$ orbital has a much larger photoemission matrix element than that of the $d_{xz}$ orbital under $p$ polarization. On the other hand, the anomalous suppression can be attributed to the matrix element effect. To show this, we calculate the photoemission dipole matrix element approximately using free-electron plane-wave states as final states and hydrogenlike wave functions as initial states (see SM Sec. VI. 1 for details [39]) [43–45]. The calculated matrix elements of the $d_{xz}$ and $p_z$ orbitals are further normalized by that of the $d_{yz}$ orbitals for direct comparison with SWR (Fig. S11 [39]). We observe a strong atomic photoemission matrix element suppression of the $p_z$ orbital around 40 eV, consistent with the experimental data. However, we cautiously note that such matrix element suppression is sensitive to the approximations of wave functions for the initial and final states (see SM Sec. VI for detailed discussion). Nevertheless, the novel spectral weight in FTS highlights the existence of $p_z$ orbital, and furthermore, serves as a strong hint for the $d_{xz}$-$p_z$ orbital character crossover.

We remark that a related spectral weight modulation of the $d_{xz}$ orbital in the inner band under the $s$ polarization has been reported in Ref. [33] with a similar $k_z$ periodicity in support of band inversion. However, our comprehensive data here reveal the more critical and unconventional elements in FeSCs, the $p_z$ orbital component under the $p$ polarization, and present a complete picture with more convincing experimental evidence indicating the inversion between the $p_z$ and $d_{xz}$ bands by (i) the identification of the $p_z$ orbital and exclusion of other mixing possibilities in FTS, (ii) the expected absence of such $p_z$ orbital in the control experiment of FeSe, (iii) the observation of SWR modulation further supporting the $d_{xz}$ and $p_z$ band crossing along the Γ-$Z$ direction, and (iv) the persistent DSS required by a nontrivial topological band structure.

With a confirmed topological band structure, we finally show a picture to reconcile the discrepancy between Figs. 1(e) and 1(f) under the framework of a tight-binding model preserving crystal symmetry (see SM Sec. VII for details [39]). Starting from the band structure calculated by the DFT [Fig. 4(a)], we make adjustments in two steps: (i) renormalize the $d$ bands by a factor of 3 with respect to the experimental $E_F$ in accordance with the in-plane dispersion [4,5,37,46] [Fig. 4(b)], and (ii) increase the $d_{xz}$-$p_z$ SOC strength as a phenomenological factor to further capture the many-body interactions [Fig. 4(c)]. See SM Sec. VII for details [39]. It is worth noting that a quantitative reproduction of experimental observations further requires an $E_F$ that locates in the gap between the $d_{xz}$ and $p_z$ bands [Fig. 4(d)] and a reduction of energy separation between the $d_{yz}$ and $d_{xz}$ bands. We note that the relative position of the holelike band with respect to the Fermi level also varies in literature [20,29]. The origin of

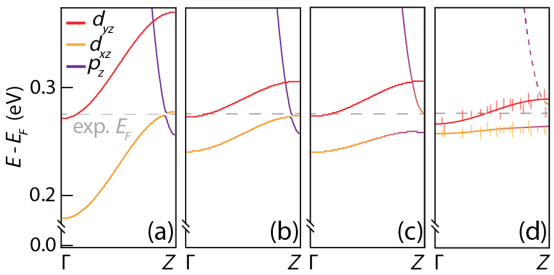


FIG. 4. Renormalization steps for the band structure. (a) DFT calculation results. (b) Renormalize the $d$ bands by a factor of 3 with respect to the experimental $E_F$ (gray dashed line). (c) A further increase of $d_{xz}$-$p_z$ SOC strength as a phenomenological measure of many-body correlations. (d) Comparison with the experimental data. The vertical lines show the experimental band tops from Fig. 1(d) and the parameters are chosen to fit the experimental data.

this discrepancy remains an ongoing research topic, with strong correlations and Mott transition effects as potential candidates [47–49]. Nevertheless, our picture vividly highlights the critical role of strong correlation in the realization of an overall topologically nontrivial band character by dramatically renormalizing the DFT predictions. This greatly reduces the energy scale and ensures the proximity of the inverted band gap to the $E_F$ for topological physics to be relevant.

In conclusion, we provide a strong case for a topological band structure in $FeTe_{0.55}Se_{0.45}$ by systematically analyzing the band dispersion and spectral weight. Our picture reconciles the discrepancy between the calculated band structure and experimental observations by necessary many-body renormalizations and provides a baseline for the further pursuit of topological physics in this system.

*Experimental methods.* FTS samples were grown by the flux method [50]. Magnetic susceptibility measurements show superconducting transition at 14 K, in agreement with the previous report [29]. The FTS data at 6 and 7 eV photon energies were collected using laser ARPES systems at Stanford University, with Scienta R4000 and R8000 analyzers, respectively. After taking each spectra on the sample, the $E_F$ is calibrated using the Fermi edge of a polycrystalline gold electrically connected to the sample. The energy resolution was 5 meV (3 meV) and the measurement temperature was 20 K (16 K) for the 6 eV (7 eV) experiments. FTS data between 15 and 25 eV data were collected at the Stanford Synchrotron Radiation Lightsource (SSRL) beam line 5-4 using a Scienta R4000 analyzer, with energy resolution at 5 meV and temperature at 16 K. The FTS data between 26 and 76 eV were collected at SSRL beam line 5-2 using a Scienta DA 30 analyzer with energy resolution at 12 meV and temperature at 16 K. The FeSe data between 26 and 52 eV are collected at SSRL beam line 5-2, on a detwinned sample [51], with energy resolution at 12 meV and temperature at 12 K. The pressure was kept below $4 \times 10^{-11}$ Torr throughout all ARPES measurements.

We acknowledge Y. He, T. P. Devereaux, D.-H. Lee, S. Kivelson, B. Moritz, and X. Dai for useful discussions. Synchrotron ARPES measurements were performed at beam line 5-2 and 5-4, Stanford Synchrotron Radiation Lightsource, SLAC National Accelerator Laboratory. The works at Stanford University and SLAC are supported by the U.S. Department of Energy, Office of Science, Office of Basic Energy Sciences, Division of Materials Sciences and Engineering, under Contract No. DE-AC02-76SF00515. Support for FTS crystal growth and characterization at Penn State is provided by the National Science Foundation through the Penn State 2D Crystal Consortium-Materials Innovation Platform (2DCC-MIP) under NSF Cooperative Agreement No. DMR-2039351. The FeSe single crystal growth at Rice is supported by the U.S. DOE, BES under Grant No. DE-SC0012311. M. G. V. thanks for support the Deutsche Forschungsgemeinschaft (DFG, German Research Foundation) GA 3314/1-1—FOR 5249 (QUAST) and partial support from European Research Council (ERC) Grant Agreement No. 101020833. The work of M. I. was funded by the European Union Next-GenerationEU/PRTR-C17.I1, as well as by the IKUR Strategy under the collaboration agreement between Ikerbasque Foundation and DIPC on behalf of the Department of Education of the Basque Government.

Y.-F. L., D.-H. L., and Z.-X. S. designed the experimental plan. Y.-F. L., S.-D. C., H. P., and J. A. S. performed ARPES experiments and data analysis. Y.-F. L. and H. P. performed matrix element calculations. M. G.-D., M. I. I., and Y.-F. L. performed DFT calculations and tight-binding modeling. Y.-L. Z. and Z.-Q. M. synthesized high-quality FTS samples. T. C., M. Y., and P.-C. D. synthesized high-quality FeSe samples. Y.-F. L., S.-D. C., M. G.-D., M. G. V., D.-H. L., and Z.-X. S. wrote the manuscript with input from all authors. J. A. S., M. H., D.-H. L., and Z.-X. S. supervised the whole project.

[1] Q. Si, R. Yu, and E. Abrahams, *High-temperature superconductivity in iron pnictides and chalcogenides*, Nat. Rev. Mater. **1**, 16017 (2016).

[2] S. He, J. He, W. Zhang *et al.*, *Phase diagram and electronic indication of high-temperature superconductivity at 65 K in single-layer* FeSe *films*, Nat. Mater. **12**, 605 (2013).

[3] J. Lee, F. Schmitt, R. Moore *et al.*, *Interfacial mode coupling as the origin of the enhancement of* $T_c$ *in* FeSe *films on* $SrTiO_3$, Nature (London) **515**, 245 (2014).

[4] M. Qazilbash, J. Hamlin, R. Baumbach, L. Zhang, D. J. Singh, M. B. Maple, and D. N. Basov, *Electronic correlations in the iron pnictides*, Nat. Phys. **5**, 647 (2009).

[5] M. Yi, Z. K. Liu, Y. Zhang *et al.*, *Observation of universal strong orbital-dependent correlation effects in iron chalcogenides*, Nat. Commun. **6**, 7777 (2015).

[6] S. Chi, F. Ye, W. Bao, M. Fang, H. D. Wang, C. H. Dong, A. T. Savici, G. E. Granroth, M. B. Stone, and R. S. Fishman, *Neutron scattering study of spin dynamics in superconducting* $(Tl, Rb)_2Fe_4Se_5$, Phys. Rev. B **87**, 100501(R) (2013).

[7] H.-H. Kuo, J.-H. Chu, J. C. Palmstrom, S. A. Kivelson, and I. R. Fisher, *Ubiquitous signatures of nematic quantum criticality in optimally doped* Fe*-based superconductors*, Science **352**, 958 (2016).

[8] D. Mou, S. Liu, X. Jia, J. He, Y. Peng, L. Zhao, L. Yu, G. Liu, S. He, X. Dong *et al.*, *Distinct Fermi surface topology and nodeless superconducting gap in a* $(Tl_{0.58}Rb_{0.42})Fe_{1.72}Se_2$ *superconductor*, Phys. Rev. Lett. **106**, 107001 (2011).

[9] C. Fang, H. Yao, W.-F. Tsai, J. P. Hu, and S. A. Kivelson, *Theory of electron nematic order in* LaFeAsO, Phys. Rev. B **77**, 224509 (2008).

[10] R. Fernandes, A. Chubukov, and J. Schmalian, *What drives nematic order in iron-based superconductors?*, Nat. Phys. **10**, 97 (2014).

[11] X.-L. Qi and S.-C. Zhang, *Topological insulators and superconductors*, Rev. Mod. Phys. **83**, 1057 (2011).
[12] P. Zhang, Z. Wang, X. Wu *et al.*, *Multiple topological states in iron-based superconductors*, Nat. Phys. **15**, 41 (2019).
[13] M. Sato and Y. Ando, *Topological superconductors: A review*, Rep. Prog. Phys. **80**, 076501 (2017).
[14] N. Hao and J. Hu, *Special issue on Topological matter: Topological quantum states of matter in iron-based superconductors: From concept to material realization*, Natl. Sci. Rev. **6**, 213 (2019).
[15] X. Shi, Z.-Q. Han, P. Richard *et al.*, $FeTe_{1-x}Se_x$ *monolayer films: Towards the realization of high-temperature connate topological superconductivity*, Bulletin **62**, 503 (2017).
[16] G. Xu, B. Lian, P. Tang, X.-L.Qi, and S.-C. Zhang, *Topological superconductivity on the surface of* Fe*-based superconductors*, Phys. Rev. Lett. **117**, 047001 (2016).
[17] N. Hao and J. Hu, *Topological phases in the single-layer* FeSe, Phys. Rev. X **4**, 031053 (2014).
[18] X. Wu, S. Qin, and Y. Liang, *Topological characters in* $Fe(Te_{1-x}Se_x)$ *thin films*, Phys. Rev. B **93**, 115129 (2016).
[19] W. Liu, L. Cao, S. Zhu *et al.*, *A new Majorana platform in an* Fe−As *bilayer superconductor*, Nat. Commun. **11**, 5688 (2020).
[20] Z. Wang, P. Zhang, G. Xu *et al.*, *Topological nature of the* $FeSe_{0.5}Te_{0.5}$ *superconductor*, Phys. Rev. B **92**, 115119 (2015).
[21] D. Hsieh, D. Qian, L. Wray, Y. Xia, Y. S. Hor, R. J. Cava, and M. Z. Hasan, *A topological Dirac insulator in a quantum spin Hall phase*, Nature (London) **452**, 970 (2008).
[22] Y. L. Chen, J. G. Analytis, J. H. Chu *et al.*, *Experimental realization of a three-dimensional topological insulator* $Bi_2Te_3$, Science **325**, 178 (2009).
[23] J. X. Yin, Z. Wu, J. H. Wang *et al.*, *Observation of a robust zero-energy bound state in iron-based superconductor* Fe(Te, Se), Nat. Phys. **11**, 543 (2015).
[24] F. Massee, P. O. Sprau, Y.-L. Wang *et al.*, *Imaging atomic-scale effects of high-energy ion irradiation on superconductivity and vortex pinning in* Fe(Se, Te), Sci. Adv. **1**, e1500033 (2015).
[25] D. Wang, L. Kong, P. Fan *et al.*, *Evidence for Majorana bound states in an iron-based superconductor*, Science **362**, 333 (2018).
[26] T. Machida, Y. Sun, S. Pyon, S. Takeda, Y. Kohsaka, T. Hanaguri, T. Sasagawa, and T. Tamegai, *Zero-energy vortex bound state in the superconducting topological surface state of* Fe(Se, Te), Nat. Mater. **18**, 811 (2019).
[27] C. Chen, K. Jiang, Y. Zhang, C. Liu, Y. Liu, Z. Wang, and J. Wang, *Atomic line defects and zero-energy end states in monolayer* Fe(Te, Se) *high-temperature superconductors*, Nat. Phys. **16**, 536 (2020).
[28] M. Chen, X. Chen, H. Yang, Z. Du, X. Zhu, E. Wang, and H.-H. Wen, *Discrete energy levels of Caroli-de Gennes-Matricon states in quantum limit in* $FeTe_{0.55}Se_{0.45}$, Nat. Commun. **9**, 970 (2018).
[29] P. Zhang, K. Yaji, T. Hashimoto *et al.*, *Observation of topological superconductivity on the surface of an iron-based superconductor*, Science **360**, 182 (2018).
[30] S. Borisenko, V. Bezguba, A. Fedorov, Y. Kushnirenko, V. Voroshnin, M. Sturza, S. Aswartham, and A. Yaresko, *Strongly correlated superconductor with polytypic 3D Dirac points*, npj Quantum Mater. **5**, 67 (2020).
[31] P. D. Johnson, H.-B. Yang, J. D. Rameau, G. D. Gu, Z.-H. Pan, T. Valla, M. Weinert, and A. V. Fedorov, *Spin-orbit interactions and the nematicity observed in the Fe-based superconductors*, Phys. Rev. Lett. **114**, 167001 (2015).
[32] S. Thirupathaiah, J. Fink, P. K. Maheshwari, V. V. Kishore, Z.-H. Liu, E. D. L. Rienks, B. Buchner, V. P. S. Awana, and D. D. Sarma, *Effect of impurity substitution on band structure and mass renormalization of the correlated* $FeTe_{0.5}Se_{0.5}$ *superconductor*, Phys. Rev. B **93**, 205143 (2016).
[33] H. Lohani, T. Hazra, A. Ribak, Y. Nitzav, H. Fu, B. Yan, M. Randeria, and A. Kanigel, *Band inversion and topology of the bulk electronic structure in* $FeSe_{0.45}Te_{0.55}$, Phys. Rev. B **101**, 245146 (2020).
[34] J. A. Sobota, Y. He, and Z.-X. Shen, *Angle-resolved photoemission studies of quantum materials*, Rev. Mod. Phys. **93**, 025006 (2021).
[35] Y. Zhang, F. Chen, C. He, B. Zhou, B. P. Xie, C. Fang, W. F. Tsai, X. H. Chen, H. Hayashi, J. Jiang *et al.*, *Orbital characters of bands in the iron-based superconductor* $BaFe_{1.85}Co_{0.15}As_2$, Phys. Rev. B **83**, 054510 (2011).
[36] M. Yi, D.-H. Lu, J.-H Chu *et al.*, *Symmetry-breaking orbital anisotropy observed for detwinned* $Ba(Fe_{1-x}Co_x)_2As_2$ *above the spin density wave transition*, Proc. Natl. Acad. Sci. U.S.A. **108**, 6878 (2011).
[37] Z. K. Liu, M. Yi, Y. Zhang, J. Hu, R. Yu, J.-X. Zhu, R.-H. He, Y. L. Chen, M. Hashimoto, R. G. Moore *et al.*, *Experimental observation of incoherent-coherent cross-over and orbital-dependent band renormalization in iron chalcogenide superconductors*, Phys. Rev. B **92**, 235138 (2015).
[38] X. P. Wang, P. Richard, Y. B. Huang *et al.*, *Orbital characters determined from Fermi surface intensity patterns using angle-resolved photoemission spectroscopy*, Phys. Rev. B **85**, 214518 (2012).
[39] See Supplemental Material at http://link.aps.org/supplemental/10.1103/PhysRevX.14.021043 for photoemission selection rule and matrix element calculations (Secs. 1 and 6, respectively); bulk band $k_z$ dispersion fit, conversion between photon energies and $k_z$, analysis of Dirac surface state signal, and spectral weight analysis (Secs. 2–5, respectively); and details for the DFT calculations and the tight-binding model (Sec. VII).
[40] A. Subedi, L. J. Zhang, D. J. Singh, and M. H. Du, *Density functional study of* FeS, FeSe, and, FeTe*: Electronic structure, magnetism, phonons, and superconductivity*, Phys. Rev. B **78**, 134514 (2008).
[41] Fazhi Yang, Giao Ngoc Phan, Renjie Zhang, Jin Zhao, Jiajun Li, Zouyouwei Lu, John Schneeloch, Ruidan Zhong, Mingwei Ma, Genda Gu *et al.*, $Fe_{1+y}Te_xSe_{1-x}$*: A delicate and tunable Majorana material*, Chin. Phys. Lett. **40**, 017401 (2023).
[42] X. L. Peng, Y. Li, X. X. Wu *et al.*, *Observation of topological transition in high-*$T_c$ *superconducting monolayer* $FeTe_{1-x}Se_x$ *films on* $SrTiO_3$ *(001)*, Phys. Rev. B **100**, 155134 (2019).

[43] S. K. Moser, *An experimentalist's guide to the matrix element in angle resolved photoemission*, J. Electron Spectrosc. Relat. Phenom. **214**, 29 (2017).

[44] X.-P. Wang, P. Richard, and Y.-B. Huang, *Orbital characters determined from Fermi surface intensity patterns using angle-resolved photoemission spectroscopy*, Phys. Rev. B **85**, 214518 (2012).

[45] R. P. Day, B. Zwartsenberg, I. S. Elfimov, and A. Damascelli, *Computational framework Chinook for angle-resolved photoemission spectroscopy*, npj Quantum Mater. **4**, 54 (2019),

[46] Y. Ming, Y. Zhang, Z.-X. Shen, and D.-H. Lu, *Role of orbital degree of freedom in iron-based superconductors*, npj Quantum Mater. **2**, 57 (2017).

[47] X. Ma, G. Wang, R. Liu, T. Yu, Y. Peng, P. Zheng, and Z. Yin, *Correlation-corrected band topology and topological surface states in iron-based superconductors*, Phys. Rev. B **106**, 115114 (2022).

[48] Minjae Kim, Sangkook Choi, Walber Hugo Brito, and Gabriel Kotliar, *Orbital selective Mott transition effects and nontrivial topology of iron chalcogenide*, Phys. Rev. Lett. **132**, 136504 (2024).

[49] Zhiguang Liao, Rong Yu, Jian-Xin Zhu, and Qimiao Si, *Orbital selective correlations for topology in* $FeTe_xSe_{1-x}$, arXiv:2306.17739.

[50] T. J. Liu, X. Ke, B. Qian *et al.*, *Charge-carrier localization induced by excess Fe in the superconductor* $Fe_{1+y}Te_{1-x}Se_x$, Phys. Rev. B **80**, 174509 (2009).

[51] H. Pfau, S. D. Chen, M. Yi *et al.*, *Momentum dependence of the nematic order parameter in iron-based superconductors*, Phys. Rev. Lett. **123**, 066402 (2019).